Journal of Materials Chemistry A

ROYAL SOCIETY OF CHEMISTRY

PAPER

View Article Online
View Journal

Cite this: DOI: 10.1039/d5ta08979d

Synergistic redox enhancement in ternary Mn–ZnFeOOH oxyhydroxides for high-performance supercapacitor applications

Palanisamy Rajkumar, [a] Vediyappan Thirumal, [a] Neela Mohan Chidambaram, [b] Maalavika S. Iyer,[c] Murugesan Prasanna,[d] Ingyung Park,[f] Soo-Hyun Kim, *[ef] Kisoo Yoo*[a] and Jinho Kim*[a]

High-performance electrode materials are vital for developing next-generation supercapacitors with enhanced energy storage capability. Mixed metal oxyhydroxides can exhibit better performance due to their high pseudo-capacitance and tunable redox activity. Thus, introducing another metal led to an enhancement of their electrochemical performance through synergistic effects and the creation of new redox-active sites. Here, Mn was incorporated into ZnFeOOH (FZ) to develop a ternary oxyhydroxide, which demonstrates the effect of Mn (FZMn-0 to FZMn-20) on the structural and electrochemical properties. Among them, FZMn-15 exhibited the most favorable characteristics, achieving a high specific capacitance of 1531 F g^{-1} at 1 A g^{-1} in a three-electrode system, while the corresponding asymmetric FZMn-15||AC device delivered 92 F g^{-1}. Furthermore, charge storage analysis indicated a diffusion-dominated process with additional capacitive contributions, highlighting the combined effect of Mn incorporation on electrochemical activity. These findings demonstrate that Mn-modified ZnFeOOH electrodes can serve as efficient and reliable materials for advanced supercapacitor applications.

Received 5th November 2025
Accepted 20th March 2026

DOI: 10.1039/d5ta08979d

rsc.li/materials-a

1 Introduction

The current lithium-ion battery technology is costly and poses environmental sustainability challenges.[1] Electrochemical capacitors (ECs) have gained considerable attention due to their promising potential in a wide range of applications, including portable electronics, electric or hybrid electric vehicles and other high-power energy systems.[2] Their exceptional characteristics such as high-power density,[3,4] rapid charging and discharging capabilities, long cycling stability and superior reliability,[5] make them a compelling choice for energy storage solutions. This has spurred extensive research into their development and optimization for next-generation energy technologies. Supercapacitors are classified into electric double-layer capacitors (EDLCs) and pseudocapacitors based on their energy storage mechanisms. EDLCs store energy through electrostatic charge accumulation, offering high power density and cycling stability, while pseudocapacitors utilize fast redox reactions to achieve higher energy densities.[6] Electrode materials for EDLCs primarily include high-surface-area carbons such as activated carbon,[7] carbon nanotubes[8,9] and graphene, which store energy through electrostatic charge accumulation. For pseudocapacitance, materials like transition metal oxides (*e.g.*, $NiMoO_4$, $CuMnO_4$),[10] conducting polymers (*e.g.* polyaniline, polypyrrole) and metal hydroxides are used, leveraging fast and reversible redox reactions for energy storage.[11,12] Another type of materials which exhibit pseudocapacitive behaviour are metal oxyhydroxides.[13] They store energy through fast and reversible redox reactions occurring at the electrode surface or near-surface regions. These materials exhibit higher energy densities compared to electric double-layer capacitors (EDLCs) and are often studied for their potential to enhance the performance of hybrid supercapacitors. Common examples include nickel oxyhydroxide (NiOOH) and cobalt oxyhydroxide (CoOOH).

Recent studies have focused on exploring oxyhydroxides as promising electrode materials for supercapacitors due to their high capacitance, stability and tunable electrochemical properties. Various metal oxyhydroxides, including cobalt, manganese, aluminum and iron-based compounds, have been investigated to enhance charge storage performance.

[a]Department of Mechanical Engineering, Yeungnam University, Gyeongsan-si, Gyeongbuk-do 38541, Republic of Korea. E-mail: kisooyoo@yu.ac.kr; jinho@ynu.ac.kr
[b]Department of Chemistry, Srimad Andavan Arts and Science College (Autonomous), Affiliated to Bharathidasan University, Tiruchirappalli, Tamil Nadu 620005, India
[c]SSN Research Centre, Sri Sivasubramaniya Nadar College of Engineering, Kalavakkam, Chennai 603110, Tamil Nadu, India
[d]Graduate School of Advanced Science and Technology, Japan Advanced Institute of Science and Technology, 1-1 Asahidai, Nomi, Ishikawa 923-1292, Japan
[e]Graduate School of Semiconductor Materials and Devices Engineering, Ulsan National Institute of Science and Technology (UNIST), Ulju-gun, Ulsan 44919, Republic of Korea. E-mail: soohyunsq@unist.ac.kr
[f]Department of Materials Science and Engineering, Ulsan National Institute of Science and Technology (UNIST), Ulju-gun, Ulsan 44919, Republic of Korea

Paunkumar *et al.* synthesized cobalt oxyhydroxide (CoOOH) *via* a facile co-precipitation method and compared its supercapacitor performance with other oxyhydroxides. CoOOH exhibited superior capacitance (1096 F g^{-1} at 25 mV s^{-1}) and excellent stability (91% retention after 5000 cycles), highlighting its potential for high-performance energy storage applications.[14] Barik *et al.* investigated the effect of cobalt doping on iron oxide for supercapacitor applications, demonstrating a facile synthesis method in ethylene glycol media. The Co-doped nano-goethite exhibited a high specific capacitance of 463.18 F g^{-1} at 0.1 A g^{-1} and excellent cycling stability, retaining 96.36% of its initial capacitance after 1000 cycles. With a band gap of 2.82 eV and a high surface area of 159.74 m^2 g^{-1}, the material showed superior electrochemical performance.[15]

Despite the promising electrochemical properties of metal oxyhydroxides, they remain less explored in supercapacitor applications due to several challenges. One key limitation is their inherent structural instability and low electrical conductivity, which hinder efficient charge transport and cycling stability. Additionally, oxyhydroxides often suffer from poor rate capability and limited electrochemical reversibility, making them less competitive than transition metal oxides and sulfides. Their synthesis methods also require precise control over composition and morphology to achieve optimal performance. Iron oxyhydroxide (FeOOH) has limitations in supercapacitor applications due to its low electrical conductivity, limited specific capacitance and poor cycling stability.[16] Its dense structure restricts ion diffusion and its brittleness can reduce electrode durability. Additionally, FeOOH operates within a narrow potential window, which limits its energy storage capacity. To address these issues, FeOOH is often doped or combined with conductive materials to improve performance. Doping in iron oxyhydroxide enhances its electrochemical performance by improving conductivity, increasing specific capacitance and stabilizing its structure for better cycling durability.[17] It modifies the electronic structure, optimizing pseudocapacitive behavior and enabling higher charge storage. Additionally, doping increases surface area and porosity, facilitating efficient ion diffusion and electrolyte penetration. Coating the doped iron oxyhydroxide on Ni foam enhances charge transfer, cycling stability and electrochemical performance. The conductive substrate improves overall capacitance, making it a promising material for high-performance supercapacitors.

Dual doping of iron oxyhydroxide (FeOOH) has been explored to improve its electrochemical performance. For example, nickel (Ni) doping of amorphous FeOOH nanosheets on ZIF-67@Ni composites significantly enhanced the oxygen evolution reaction (OER) performance.[18] A study also synthesized a dual-phase cobalt sulfide/cobalt oxyhydroxide ($Co_{1-x}S$/$HCoO_2$) nanostructure on iron carbide-integrated porous carbon nanofibers. This dual-phase design enhanced the specific capacitance to 1724 F g^{-1} at 1 A g^{-1}, with improved rate capability and exceptional cycling stability.[19]

Dual doping of FeOOH with manganese (Mn) and zinc (Zn) enhances its electrochemical performance by promoting synergistic effects that improve conductivity, stability and charge storage. Mn doping boosts electrical conductivity, while Zn stabilizes the structure, preventing degradation during cycling. This dual doping also increases surface area and porosity, leading to higher specific capacitance and better cycling stability, making FeOOH a promising material for high-performance supercapacitors. A study by Li *et al.* investigated Mn-doped FeOOH's adsorption performance on heavy metals, finding that Mn doping increased the specific surface area and adsorption capacity for Cd(II), Ni(II) and Pb(II) by 18%, 17% and 40%, respectively, compared to undoped FeOOH.[20] The choice of Zn and Mn as co-dopants is motivated by their distinct yet complementary physicochemical characteristics. Zn^{2+} has an ionic radius comparable to that of Fe^{3+}, allowing it to substitute into the FeOOH lattice with minimal structural strain.[21] Such substitution helps preserve the overall framework while subtly adjusting lattice parameters, which can facilitate ion transport.[22] In addition, Zn^{2+} exhibits a fully filled $3d^{10}$ configuration and is therefore largely electrochemically inactive within the typical operating voltage range. This feature enables Zn to function primarily as a structural supporter rather than a redox-active center.[23] Additionally, a study by AL-Jawad *et al.* prepared Fe-doped, Mn-doped and Fe/Mn co-doped titanium dioxide (TiO_2) nanoparticles to enhance photocatalytic activity.[24] While specific studies on dual doping of iron oxyhydroxide (FeOOH) with Mn and Zn are limited, research on doping FeOOH with Mn has demonstrated enhanced properties. These studies suggest that doping FeOOH with Mn can enhance its properties and similar approaches with Zn doping could potentially yield beneficial effects.

The relatively stable Zn–O coordination strengthens the local bonding environment, suppresses excessive lattice distortion, and reduces structural collapse or Fe dissolution during cycling, thereby improving long-term stability.[25] In contrast, Mn plays a more active electronic role. Owing to its multiple accessible oxidation states (Mn^{2+}/Mn^{3+}/Mn^{4+}), Mn incorporation introduces additional redox centers that contribute to enhanced charge storage.[26,27] Meanwhile, the different electronic configuration of Mn alters the local electronic structure of FeOOH, which may reduce the band gap and promote electron transport through Fe–O–Mn interactions. Such electronic modulation improves charge-transfer kinetics and overall conductivity. Moreover, Mn doping can induce lattice defects or oxygen vacancies, which increase the number of electrochemically active sites and improve ion diffusion dynamics.[28,29] Consequently, the co-doping strategy integrates the structural stabilization effect of Zn with the electronic activation function of Mn, leading to synergistically enhanced conductivity, structural robustness, and electrochemical performance of FeOOH.

This work investigates the strategic tuning of Mn in zinc-stabilized iron oxyhydroxide (FeOOH) to develop ternary oxyhydroxides which enhance its electrochemical performance for supercapacitor applications. While Zn is introduced at a fixed concentration to stabilize the structure and maintain conductivity, varying amounts of Mn are incorporated to systematically study their influence on the material's morphology, conductivity and charge storage behavior. The combination of constant Zn and variable Mn doping is intended to leverage the

individual and combined effects of these elements, promoting improved surface area, structural integrity and charge transfer kinetics. This approach addresses a less-explored area in current research by optimizing Mn doping in the presence of Zn, aiming to develop a non-noble multi-metal oxyhydroxides electrode materials with superior performance and long-term stability for energy storage applications.

2 Experimental

2.1 Materials

Analytical grade zinc acetate dihydrate ($Zn(CH_3COO)_2 \cdot 2H_2O$), iron nitrate nonahydrate ($Fe(NO_3)_3 \cdot 9H_2O$) and manganese acetate tetrahydrate ($Mn(CH_3COO)_2 \cdot 4H_2O$) were used as precursor sources for Zn^{2+}, Fe^{3+} and Mn^{2+} ions, respectively.

2.2 Synthesis of ternary oxyhydroxides (FZMn-*x*) nanostructures

A series of Mn-doped FeOOH nanostructures with a constant Zn content and varying Mn doping levels (1, 5, 10, 15 and 20%) were synthesized *via* a simple co-precipitation method. Iron nitrate nonahydrate ($Fe(NO_3)_3 \cdot 9H_2O$), manganese acetate tetrahydrate ($Mn(CH_3COO)_2 \cdot 4H_2O$) and zinc acetate dihydrate ($Zn(CH_3COO)_2 \cdot 2H_2O$) were used as precursor salts for Fe^{3+}, Mn^{2+} and Zn^{2+} ions, respectively. 0.1 M of $Fe(NO_3)_3 \cdot 9H_2O$ was dissolved in 100 mL of deionized water under constant magnetic stirring. A fixed concentration of 0.005 M $Zn(CH_3COO)_2 \cdot 2H_2O$ was added to the solution as a stabilizing co-dopant. To introduce Mn^{2+} doping, varying concentrations of $Mn(CH_3COO)_2 \cdot 4H_2O$ – 0.001 M, 0.005 M, 0.010 M, 0.015 M and 0.020 M were added to prepare samples with 1, 5, 10, 15 and 20% Mn doping, respectively. The mixed solution was stirred for 30 minutes at room temperature to ensure complete dissolution of all metal precursors. 1 M NaOH solution was then added dropwise under vigorous stirring until the pH of the reaction mixture reached ~11, initiating the co-precipitation of FeOOH with incorporated dopant ions. The mixture was maintained at 80 °C for 3 hours to facilitate the growth of doped FeOOH nanostructures. The resulting precipitate was separated by centrifugation and thoroughly washed several times with deionized water and ethanol to remove residual ions and by-products. The obtained product was dried at 100 °C for 12 hours in a hot air oven and subsequently ground using an agate mortar to obtain uniform fine powders. The sample code in general is FZMn-*x*, where F is FeOOH (base material), Z is the constant Zn doping (5%), Mn-*x* is *x* mol% Mn doping. In this work we have labelled the samples as FZMn-0, FZMn-1, FZMn-5, FZMn-10, FZMn-15 and FZMn-20.

The synthesized Mn-doped @ Zn-stabilized Fe-oxyhydroxide samples were stored in airtight containers for further physico-chemical and electrochemical characterization. This synthesis strategy enables controlled tuning of Mn doping while maintaining structural stability through a constant Zn incorporation under mild processing conditions.

3 Results and discussion

The samples are examined for their phase purity using X-ray Diffraction (XRD) analysis, as shown in Fig. 1. All diffraction patterns corresponds to JCPDS no: 00-034-1266, with no detectable impurities.[30] Subtle peaks corresponding to (110), (200), (400), (420) and (321) diffraction planes can be observed at 11.8°, 16.8°, 33°, 38° and 42.8° 2θ values. The prominent peak at 26.6°, 35.1° and 55.7° corresponds to (310), (211) and (521) planes. With an increase in Mn concentration, the overall diffraction pattern remains unchanged indicating that the incorporation of Mn does not alter the host crystal structure, but is accommodated in the lattice. However, a slight decrease in peak intensity and broadening of peaks can be observed for Mn doped samples, which suggests lattice distortion. This reduction in peak intensity can be attributed to lattice distortion and increased structural disorder caused by the substitution of Fe^{3+} with larger Mn^{2+} ions. As Mn doping increases, the disruption of crystallographic order becomes more pronounced, leading to a decline in overall crystallinity and a weakening of preferential crystal orientation. These changes suggest successful incorporation of Mn and its significant influence on the FeOOH lattice structure.

The surface morphology of the synthesized samples was investigated using scanning electron microscopy (SEM), as shown in Fig. 2. Fig. 2a displays the SEM image of pure FZMn-0, revealing nanorods that are densely agglomerated into a reef-like architecture. A higher magnification image in Fig. 2b confirms the formation of well-defined nanorods, characteristic of the pristine FeOOH sample. Upon doping with 1% of Mn (FZMn-1) (Fig. 2c), noticeable morphological changes are observed. The openness of the original reef-like structure begins to diminish, as the spaces between the nanorods become partially filled with secondary nanostructures, suggesting the incorporation of dopants into the matrix. Fig. 2d further

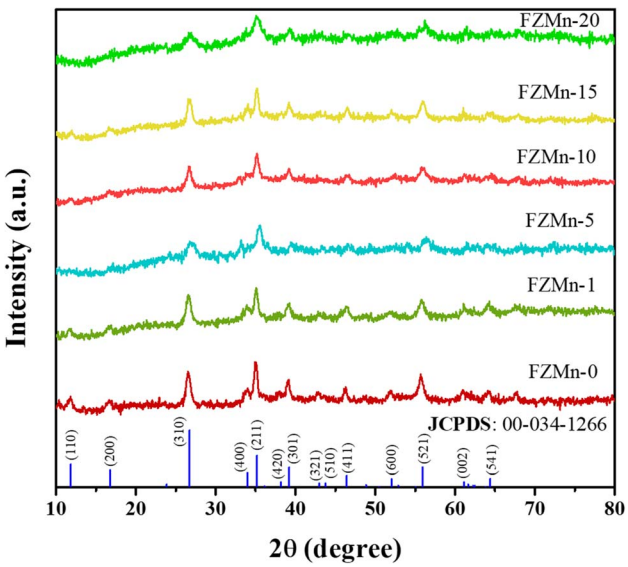

Fig. 1 XRD patterns of all the prepared samples.

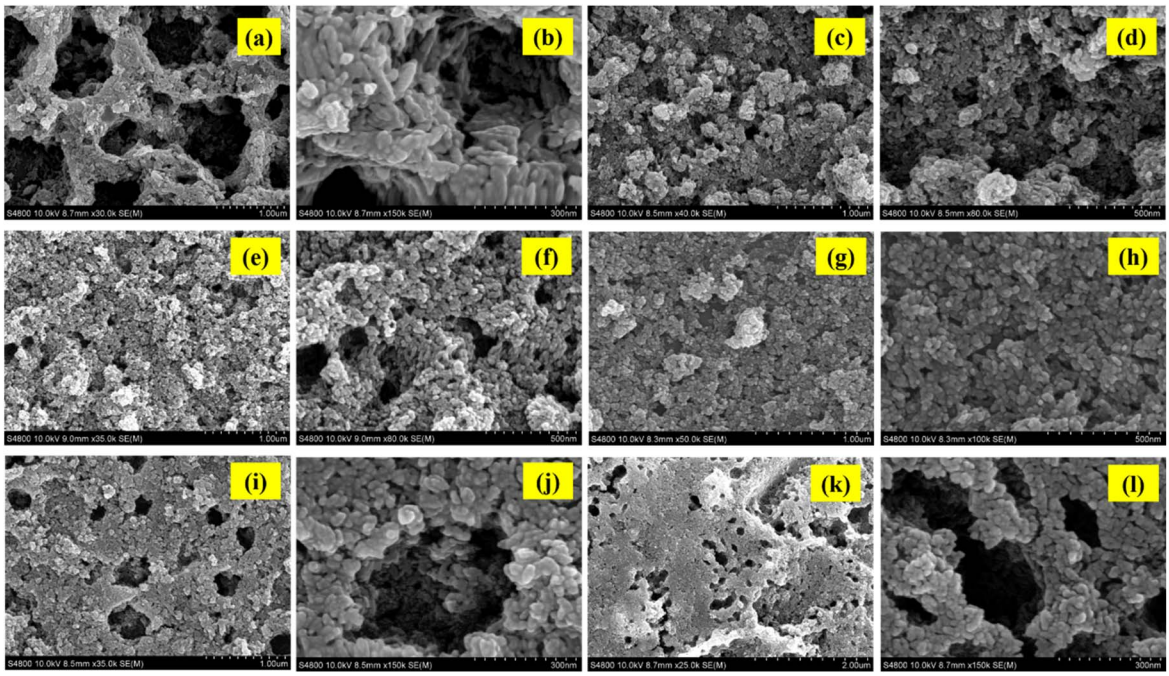

Fig. 2 SEM images of all the prepared samples: (a and b) FZMn-0, (c and d) FZMn-1, (e and f) FZMn-5, (g and h) FZMn-10, (i and j) FZMn-15 and (k and l) FZMn-20 respectively.

highlights that although some regions remain open, the structural pores are partially enclosed.

As the doping level is increased to 5% (Fig. 2e), the open porous network becomes more compact, with dopant-derived nanostructures occupying the voids within the reef-like morphology. Interestingly, Fig. 2f reveals a bimodal pore distribution, where both large and small pores coexist, potentially enhancing electrolyte accessibility and ion transport. Further increase in dopant concentration to 10% (Fig. 2g) results in a more pronounced agglomeration of the nanostructures. The nanorods begin to merge, forming larger, nanosphere-like aggregates. At 15% doping (Fig. 2i), a hybrid morphology emerges, characterized by the coexistence of small and large pores, along with distinct nanospheres adhering to the surface of FZMn-0 nanorods, indicating strong interaction between the host and the dopant phases. At the highest doping level of 20% (Fig. 2k), the morphology transitions into a more compact, cloudy, plateau-like structure with a relatively reduced pore volume. The low magnification image reveals smaller pores, while the high magnification image (Fig. 2l) confirms the presence of nano-spherical features positioned adjacent to the FZMn-0 nanorods. Overall, the gradual evolution in morphology from open reef-like nanorod networks to more compact and spherical architectures suggests that Mn and Zn doping significantly influences the surface structure of Fe-oxyhydroxides. The presence of interconnected porous features throughout the series is advantageous for electrolyte diffusion and ion transport, which can positively impact the electrochemical performance of the material.

For a better understanding, Transmission Electron Microscope (TEM) were used to study the morphology of FZMn-15. Fig. 3a shows a low-magnification TEM image of the synthesized Zn-stabilized, FeOOH sample (FZMn-0). The image clearly reveals rod-like nanostructures distributed across the field of view. These nanorods are seen to aggregate into clustered arrangements, with some aligning in parallel stacks or bundles. The overall morphology confirms successful formation of anisotropic, 1D nanostructures typical of FeOOH. Fig. 3b presents a high-magnification view of individual nanorods with their lengths measured, showing values such as 49.35 nm, 55.42 nm, 65.77 nm, 70.64 nm and 75.23 nm. This confirms that the nanorods are uniform in shape, typically in the 50–75 nm length range, indicating a relatively narrow size distribution. These dimensions are ideal for supercapacitor applications, as shorter diffusion paths enhance charge transport. The Selected Area Electron Diffraction (SAED) pattern (Fig. 3c) depicts the presence of concentric diffraction rings with bright, discrete spots indicates that the sample is polycrystalline in nature. The sharpness and intensity of the rings suggest high crystallinity. In addition, the SAED pattern shows distinct concentric rings, with measured diameters of 74.80 nm and 173.70 nm corresponding to interplanar spacings of approximately 2.56 Å and 1.45 Å, which are indexed to the (400) and (002) planes of β-FeOOH, respectively. Fig. 3d presents a low-magnification TEM image showing uniformly distributed nanorods of Zn-stabilized FeOOH co-doped with Mn. The nanorods appear to be well-separated and randomly oriented, without significant aggregation, suggesting good dispersibility and growth control. This uniform nanostructure supports the idea of consistent doping and homogeneous nucleation during synthesis. Fig. 3e shows a high-resolution image of the same nanostructures. Several nanorods have been measured, revealing lengths ranging from

~40 to 57 nm. These measurements indicate a relatively narrow size distribution, which suggests controlled growth kinetics during the co-precipitation process. The decrease in length of nanorods when compared to undoped sample can be attributed to Mn-induced inhibition of crystal growth, which is a typical transition metal doping behavior.[31] Fig. 3f shows the SAED pattern of the FZMn-15 sample. The presence of bright concentric rings confirms that the sample is polycrystalline in nature. The rings are well-defined with discrete spots, indicating good crystallinity. The two ring measurements observed in the SAED pattern (Fig. 3f) correspond to spatial frequencies of 3.23 nm^{-1} and 5.13 nm^{-1}. These values closely match with the diffraction planes (310) and (411) of β-FeOOH respectively. The well-defined rings in SEAD pattern indicates the polycrystalline nature of FZMn-15 sample. Overall, the TEM results matched with XRD results, confirming the successful development of ternary oxyhydroxides (FZMn-*x*).

The elemental composition and valence state of the sample is analysed using XPS technique and the results are shown in Fig. 4. Fig. S1a shows the survey spectra of FZMn-15 with distinct peaks at 1020 eV, 710 eV, 660 eV, 531 eV and 285 eV corresponding to Zn 2p, Fe 2p, Mn 2p, O 1s and C 1s states. Fig. S1b shows the high-resolution spectra of C 1s corresponding to adventitious carbon (AdC). The presence of C=C carbon is evident from the peak at 284.6 eV. A peak at 285.6 eV can be attributed to C–C bond, while the peak at a higher binding energy of 288.5 eV can be attributed to O–C=O.[32] These carbon species enrich the interaction with metal oxide components. In the deconvoluted spectra of Zn 2p (Fig. 4a) there are two main characteristics peaks which correspond to spin–orbit doublet of Zn 2p electrons. The peak at 1021.8 eV can be attributed to Zn $2p_{3/2}$, while Zn $2p_{1/2}$ peak can be observed at 1044.9 eV, with typical spin–orbit splitting of 23.1 eV.[33] These binding energy values confirm the presence of Zn^{2+} oxidation state. The XPS spectra of Mn 2p is shown in Fig. 4b, which is deconvoluted into four peaks at 641 eV, 642.7 eV, 653.9 eV and 657.2 eV. These can be assigned to Mn^{3+} ($2p_{3/2}$), Mn^{4+} ($2p_{3/2}$), Mn^{3+} ($2p_{1/2}$) and Mn^{4+} ($2p_{1/2}$) respectively, with the spin–orbit splitting 12 eV.[34] In addition, distinct satellite peaks can be observed, which indicates characteristic peak of Mn^{3+} and Mn^{4+}. These features collectively indicate the presence of mixed-valance state of manganese, which might play crucial role in enhancing charge storage capability. Fig. 4c shows the high-resolution spectra of Fe 2p state, which displays two major peaks corresponding to spin–orbit doublet of Fe 2p electrons. The Fe $2p_{3/2}$ peak at 710.7 eV and Fe $2p_{1/2}$ peak at 724.2 eV has a spin–orbit splitting of 13.5 eV. The peak at 710.5 eV can be assigned to Fe^{2+} species and the peak at 713.1 eV can be assigned to Fe^{3+} state.[35] Also, satellite peaks can be observed here which is characteristic peak of Fe^{3+} indicating the presence of the same. The coexistence of Fe^{2+} and Fe^{3+} oxidation states as revealed by the deconvoluted spectra is beneficial for its electrochemical performance. The deconvolution spectra of pristine FeOOH is shown in Fig. S2, a slight shift in peaks towards higher binding energy can be observed for Fe_{2p} in FZMn-15 sample. This can be attributed to the increment in the electron density around Fe due to doping.[36] The O 1s spectra with multiple deconvoluted peaks that reflects different oxygen states is shown in Fig. 4d. The dominant peak

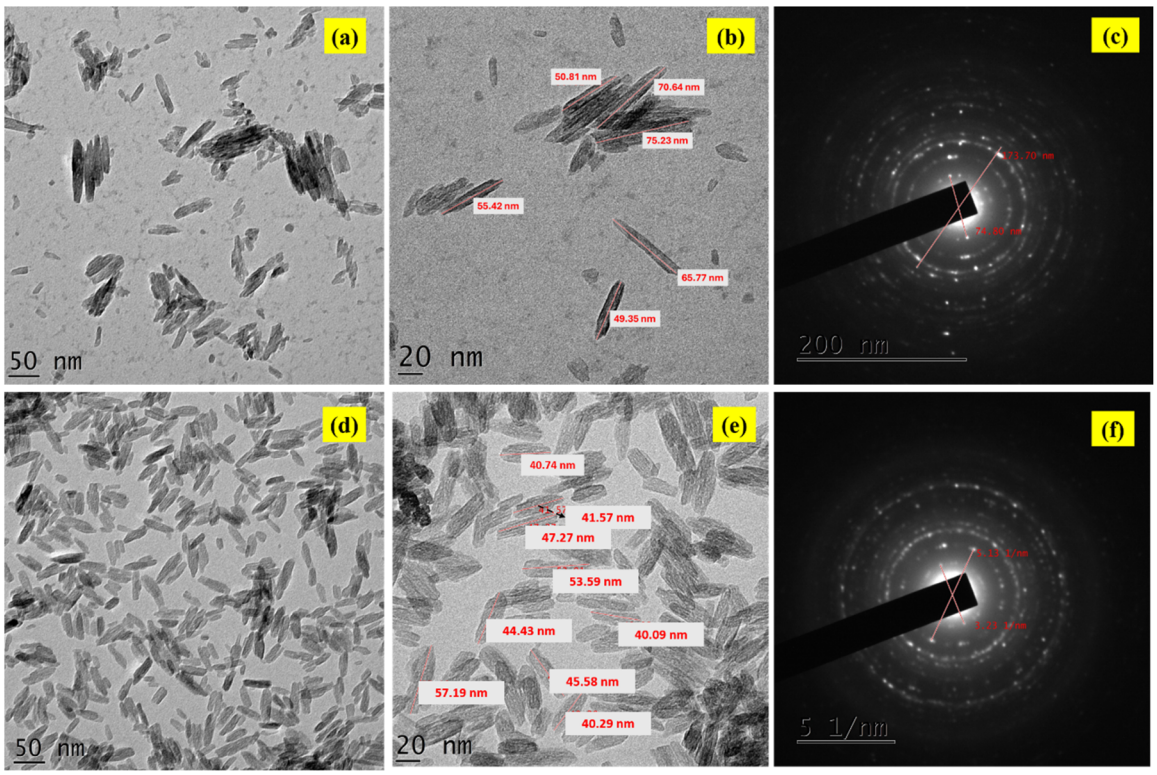

Fig. 3 (a and b) TEM images and (c) SAED pattern of FZMn-0 sample; (d and e) TEM images and (f) SAED pattern of FZMn-15 sample.

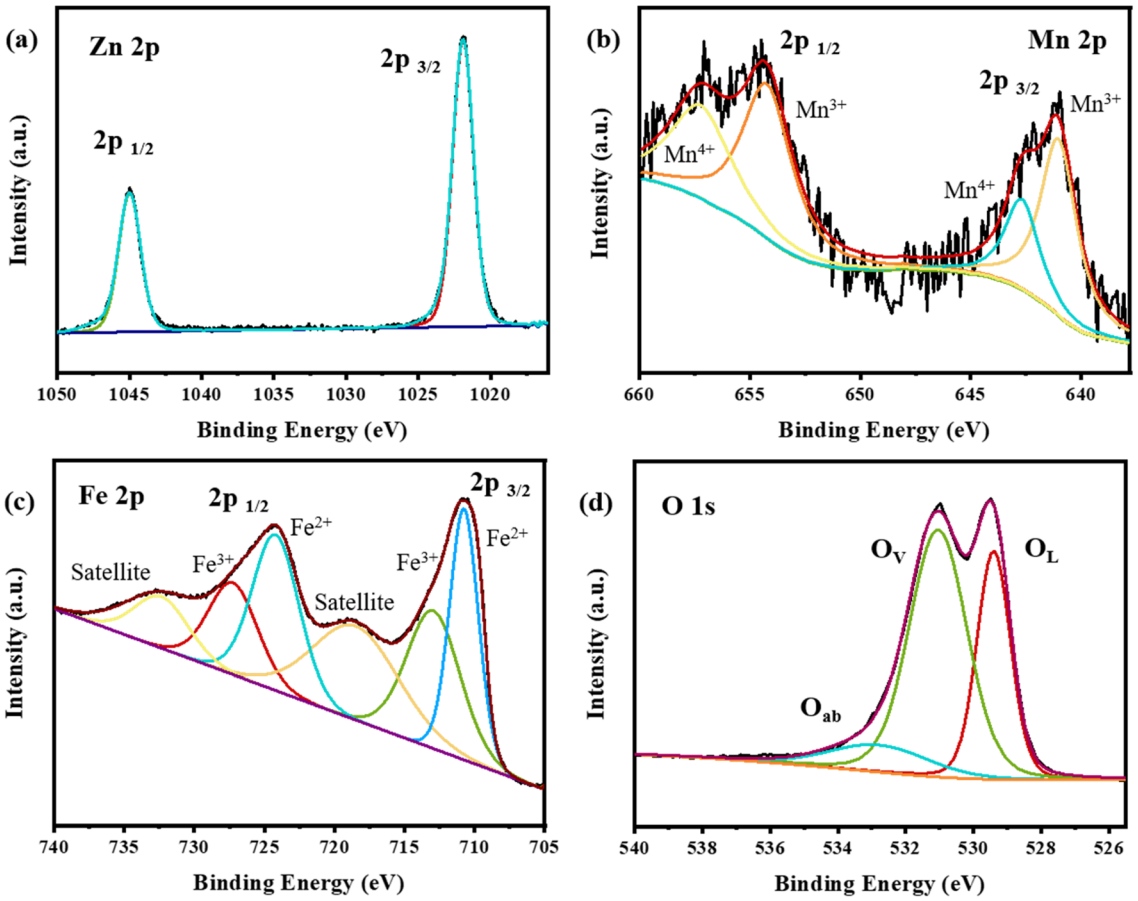

Fig. 4 Deconvoluted XPS spectra of (a) Zn 2p, (b) Mn 2p, (c) Fe 2p and (d) O 1s of the FZMn-15 sample.

at 529 eV can be attributed to the lattice oxygen (O_L). The peak at 531 eV corresponds to oxygen vacancies (O_V) which are known to enhance the redox activity. The binding energy peak at 533 eV can be assigned to surface-absorbed oxygen species (O_{ab}). The coexistence of lattice oxygen, oxygen vacancy and surface absorbed oxygen highlights the capability of ZFMn-15 for fast charge transfer and improved electrochemical performance.[37]

4 Electrochemical measurements

Fig. 5 shows the cyclic voltammetry (CV) profile, depicting the electrochemical behavior of the electrodes under consideration. The CV curves exhibits a redox feature suggesting pseudocapacitive charge storage mechanism. The presence of anodic and cathodic peaks can be attributed to reversible faradaic redox transitions of the electroactive species. With the increase in scan rate from 10 mV s^{-1} to 100 mV s^{-1} there is an increase in area enclosed by the curve, which confirms enhanced charge storage with faster ion intercalation/deintercalation and surface reactions. Also, the CV curve retains its characteristic shape demonstrating excellent rate capability and rapid ion transport kinetics. At lower scan rates, the redox peaks are sharper and more pronounced, this indicates efficient diffusion of electrolyte ions into the bulk of the electrode, whereas at higher scan rates a slight distortion and peak shift are observed, which can be attributed to polarization effects and limited ion diffusion. The nearly overlapping nature of CV curves at higher scan rates indicates the electrochemical stability and reversibility of the electrodes.

For the electrodes FZMn-0, FZMn-1, FZMn-5, FZMn-10, FZMn-15 and FZMn-20, the maximum current responses recorded from the CV profiles were 128, 134, 146, 159, 209 and 162 mA, respectively. A gradual increase in current density is observed with increasing Mn content up to FZMn-15, which indicates improved electrical conductivity and enhanced redox activity due to the incorporation of Mn. The sharp rise to 209 mA for FZMn-15 (Fig. 5e) demonstrates the optimal concentration of Mn, where a synergistic effect between the host matrix and Mn species significantly enhances charge transfer kinetics and electroactive site availability. However, a decrease of current density to 162 mA for FZMn-20 (Fig. 5f) suggests that excessive Mn loading might lead to agglomeration or blockage of active sites, thereby reducing the effective electrochemical activity. This trend confirms that the electrode composition plays a crucial role in tuning ion accessibility and charge storage efficiency. The comparison of CV curves as shown in Fig. 5g clearly reveals that compositional tuning markedly influences electrochemical performance, with FZMn-15 electrode offering the highest current density. Fig. 5h depicts the plot of scan rate *versus* current density values derived from the

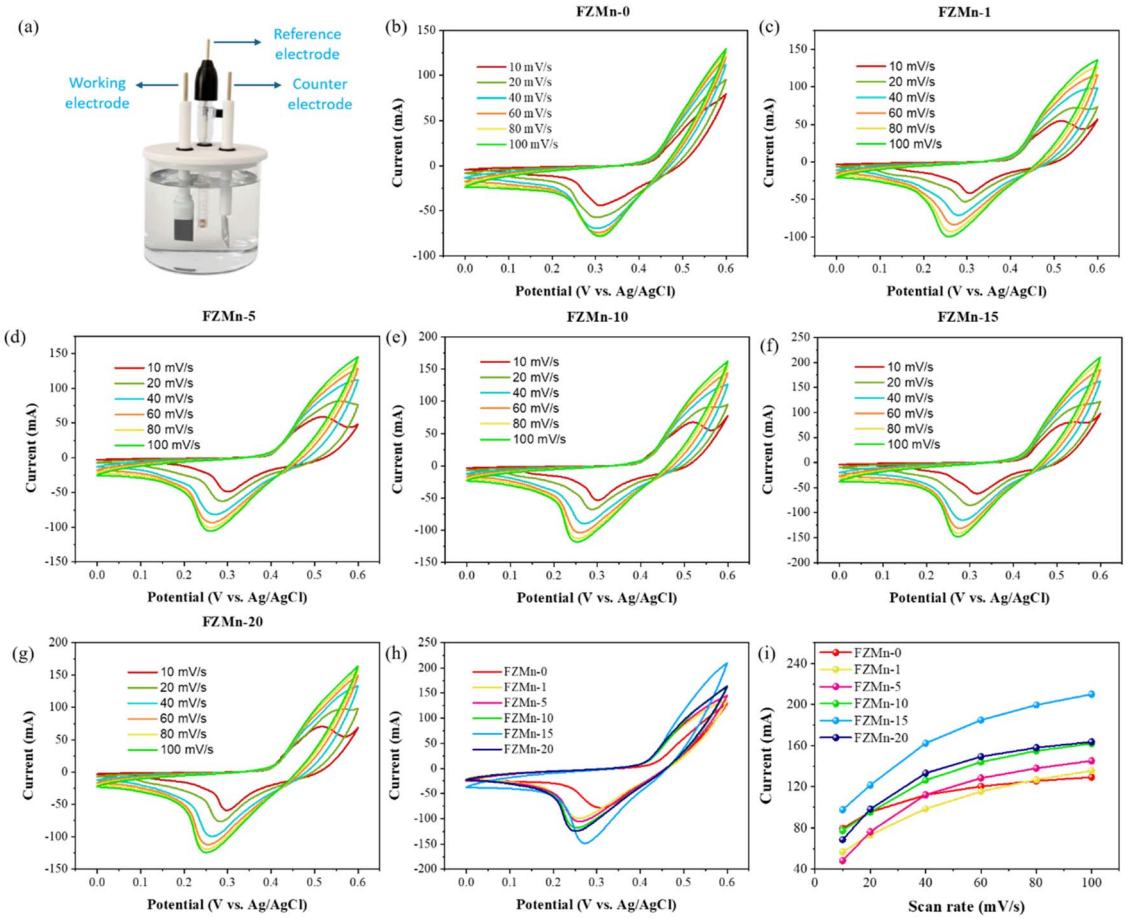

Fig. 5 (a) Schematic of three-electrode setup; (b–g) CV curves with different scan rates of FZMn-0, FZMn-1, FZMn-5, FZMn-10, FZMn-15 and FZMn-20 electrodes respectively; (h) comparison of CV curves for all electrodes at a scan rate of 100 mV s^{-1} and (i) scan rate *vs.* current graph of all the electrodes.

CV curves of the electrodes. A consistent increase in current density with scan rate is observed, with FZMn-15 showing the highest response, reflecting its superior electrochemical activity, which can be attributed to the optimized Mn content, which provides the highest density of electrochemically active sites and an optimal Mn^{3+}/Mn^{4+} redox balance. This composition enhances electronic conductivity and charge-transfer kinetics while maintaining favorable ion diffusion and structural stability. At lower Mn contents, the number of active redox sites is insufficient, whereas higher concentrations lead to structural disorder and increased charge-transfer resistance, resulting in inferior electrochemical performance.

To gain further insight into the charge storage mechanism of the electrode materials, *b* value analysis was carried out based on the power law relationship as given in eqn (6) to (8) (SI file). The *b* value is obtained from the slope of the linear fit of log(*i*) *versus* log(*v*), where *i* is the peak current and *v* is the scan rate, as illustrated in Fig. 6a. The calculated *b* values were found to be 0.32 for the cathodic peak and 0.38 for the anodic peak. These values clearly indicate that the charge storage mechanism in the electrode is predominantly governed by diffusion-controlled intercalation processes rather than surface-driven capacitive contributions. This diffusion-dominated behavior is consistent with the prolonged discharge times observed in the GCD profiles. Fig. 6b presents the plot of $v^{1/2}$ *vs.* $i_p/v^{1/2}$, which is used to quantitatively distinguish the capacitive and diffusion-controlled charge storage contributions. The slope of the fitted line corresponds to the diffusion-controlled component (k_2), while the intercept represents the capacitive contribution (k_1). This analysis enables the relative percentage of capacitive and diffusion-controlled processes to be estimated at each scan rate. The clear linearity observed in the plot suggest that the electrode exhibits a dominant diffusion-controlled behavior with a smaller but noticeable capacitive contribution. Fig. 6c illustrates the comparative bar diagram of capacitive and diffusion-controlled contributions at different scan rates. At lower scan rates, the capacitive contribution dominates as high as 82%, while the diffusion-controlled process accounts for only about 17%. This indicates that under slow sweep conditions, ions have sufficient time to access both surface active sites and shallow under the surface regions, resulting in higher capacitive storage. However, as the scan rate increases, the capacitive contribution decreases steadily to 32%, while the diffusion-controlled process rises sharply to 67%. This transition occurs

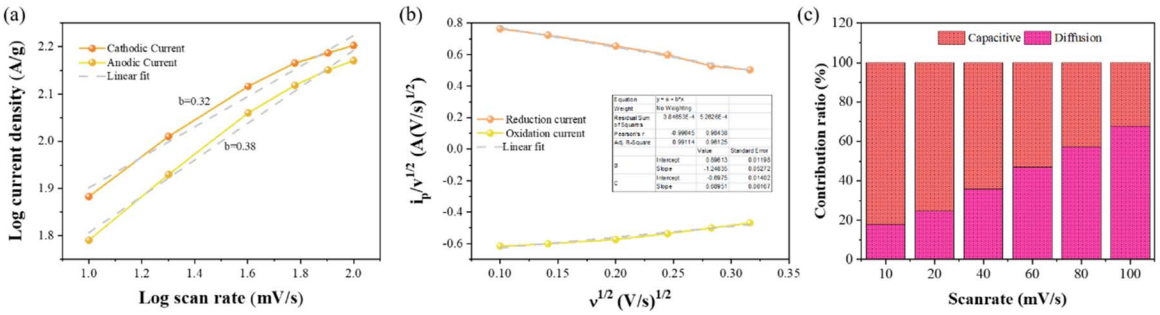

Fig. 6 (a) Linear fit of log(v) and log(i), (b) linear fit of $v^{1/2}$ *vs.* $i_p/v^{1/2}$,and (c) a percentage of the diffusion-controlled and capacitive controlled processes of FZMn-15 electrode.

because at higher scan rates, ion transport becomes kinetically limited, restricting access to deeper active sites and favoring diffusion-controlled intercalation pathways.[38] Such behavior clearly demonstrates the hybrid nature of the charge storage mechanism in the electrode, where surface capacitive effects dominate at low scan rates, whereas bulk diffusion processes govern the kinetics at higher scan rates.

In this context, the formation of oxyhydroxide phases is critical to this hybrid response. Oxyhydroxides provide redox-active metal centers (M–O/M–OH) that readily undergo reversible faradaic reactions, contributing to surface pseudocapacitance at low scan rates. Simultaneously, their layered and hydrated structure allows partial ion insertion into near-surface lattice sites, which becomes increasingly diffusion-controlled at higher scan rates. Thus, oxyhydroxides act as an electrochemically adaptive phase, bridging surface-controlled capacitive behavior and bulk diffusion-driven charge storage, and thereby regulating the overall electrochemical kinetics of the electrode.

Fig. 7(a–f) shows the galvanostatic charge discharge profiles of the samples in 3 electrode system. Initially, GCD measurements were conducted over a 0–0.6 V window for all samples. However, at the lower current density of 1 A g^{-1}, the GCD curves did not reach full charge/discharge due to low coulombic efficiency.[39] To ensure consistent and reliable measurements, the potential window was adjusted to 0–0.5 V for all electrodes. All samples exhibit quasi-triangular plots indicating a combination of electric-double layer and pseudocapacitive contribution. The discharge time increases progressively from FZMn-0 to FZMn-15, indicating enhanced specific capacitance due to the increased availability of electroactive sites and improved conductivity. Specifically, FZMn-0 exhibits a discharge time of 878 s, which increases to 1100 s for FZMn-1, 1346 s for FZMn-5, 1686 s for FZMn-10 and reaches a maximum of 1934 s for FZMn-15. A slight decrease is observed for FZMn-20, with a discharge time of 1509 s. This decrease at FZMn-20 indicates that overloading with Mn could hinder efficient ion transport or reduce the effective surface area, emphasizing the importance of an optimal Mn content for maximizing electrochemical performance. The specific capacitance values calculated from the GCD plots at a current density of 1 A g^{-1} are 849, 949, 1147, 1294, 1531 and 1417 F g^{-1} for FZMn-0, FZMn-1, FZMn-5, FZMn-10, FZMn-15 and FZMn-20, respectively. At a higher current density of 10 A g^{-1}, the specific capacitance values decrease to 364, 538, 656, 710, 896 and 790 F g^{-1} for FZMn-0, FZMn-1, FZMn-5, FZMn-10, FZMn-15 and FZMn-20, respectively. Although a reduction in capacitance with increasing current density is expected due to insufficient time for ion diffusion into the deeper pores, FZMn-15 still retains a substantial fraction of its capacitance, underscoring its superior rate capability compared to the other electrodes. Fig. 7g shows the comparative GCD profiles of all the electrodes under investigation; herein, we can see that the discharge times increase progressively with Mn incorporation, with FZMn-15 exhibiting the longest discharge duration, indicative of its highest specific capacitance. In contrast, FZMn-20 shows a shorter discharge time compared to FZMn-15, suggesting that excessive Mn content may hinder effective charge storage. Fig. 7h illustrates the plot of current density *vs.* specific capacitance for all electrodes. The capacitance decreases with increasing current density, yet FZMn-15 maintains the highest values across all rates, confirming its excellent rate capability. Furthermore, the FZMn-15 electrode exhibits superior performance compared to earlier reported results (Table S1), confirming its enhanced electrochemical properties. Fig. S3(a) shows the Nyquist plots of all the samples investigated, illustrating the variation of impedance with Mn content. All plots display a semicircular arc in the high-frequency region followed by a linear tail in the low-frequency region, characteristic of faradaic charge-transfer and diffusion-controlled processes, respectively. The appropriate equivalent circuit diagram is shown in the inset of Fig. S3(a). Among all samples, FZMn-15 exhibits the smallest semicircle, indicating the lowest R_{ct} value and thus superior charge transfer kinetics and electrical conductivity. Moreover, FZMn-15 electrode shows lower solution resistance than that of other electrodes, further confirming its enhanced electrochemical performance. The reduced impedance with optimized Mn incorporation confirms enhanced electrochemical activity and improved ion diffusion at the electrode–electrolyte interface.

To further assess the practical applicability of the superior electrode, an asymmetric two electrode device was fabricated with FZMn-15 as the positive electrode and activated carbon as negative electrode. This configuration was designed to exploit the high capacitance of FZMn-15 along with the electric double layer capacitance of carbon. The operating potential ranges

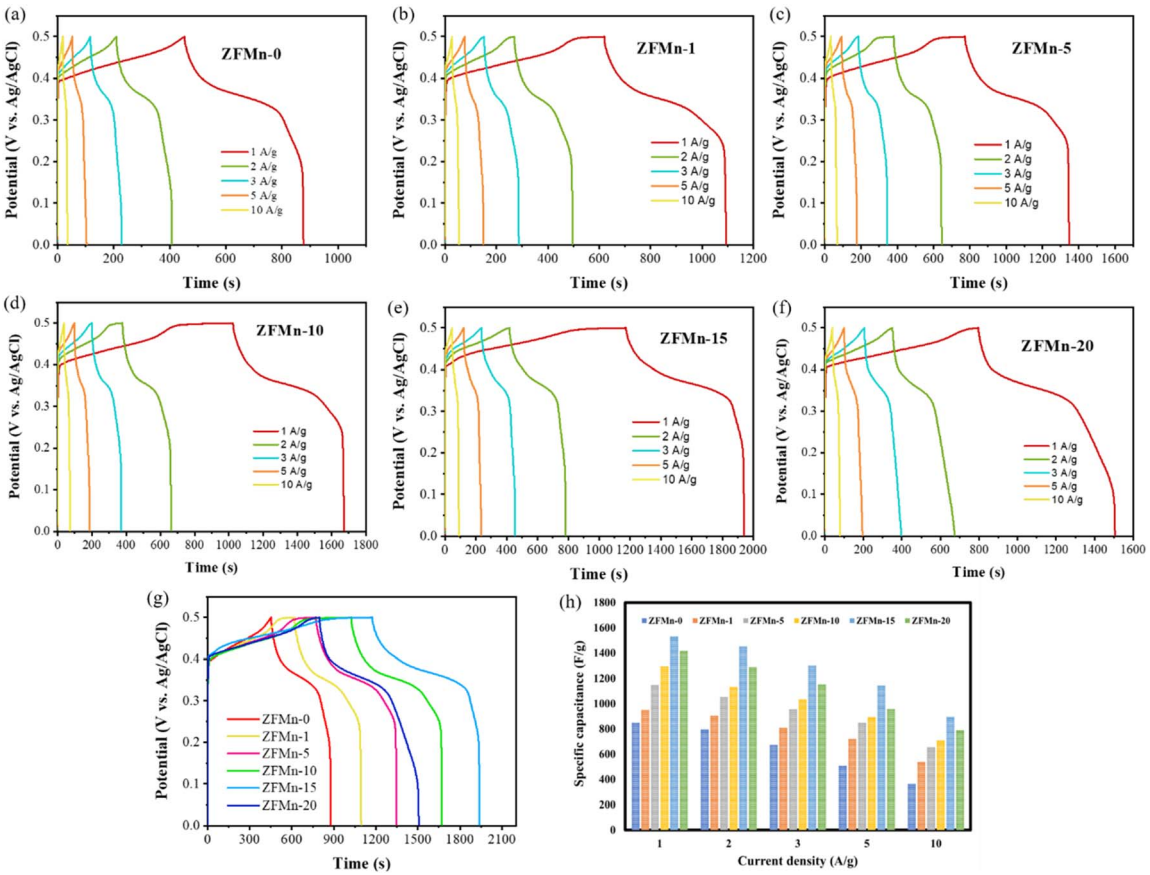

Fig. 7 (a–f) CV curves all the prepared electrodes with different current density; (g) comparison of GCD curves at a current density of 1 A g^{-1} and (h) comparison of current density *vs.* specific capacitance graph of all the studied electrodes.

determined from the three-electrode system was 0 to 0.6 V for the positive electrode and −1 to 0 V for the negative electrode, as shown in Fig. S4. This extends the operating voltage window and enhances the overall energy storage capability of the FZMn-15||AC device. The highest current response from the CV measurements was recorded at a scan rate of 100 mV s^{-1}, reaching a value of 5.6 mA (Fig. 8b). The GCD profile of the FZMn-15||AC device exhibits a distorted triangular shape (Fig. 8c), which indicates the combined contribution of electric double-layer capacitance and faradaic redox reactions, confirming its pseudocapacitive nature. From the discharge curve, the specific capacitance was calculated to be 92 F g^{-1}, demonstrating the effective charge-storage capability of the fabricated asymmetric device. At a high current density of 10 A g^{-1}, the device delivers a discharge time of 308 s, reflecting its ability to retain a considerable charge storage capacity even under fast charge–discharge conditions. A comparative analysis presented in Table S2 reveals that the FZMn-15||AC device exhibits enhanced electrochemical performance compared to earlier reported devices, confirming its promising potential for high-performance energy storage applications. The Nyquist plots of the FZMn-15||AC device recorded before and after cycling (Fig. 8d) do not exhibit a distinct semicircle in the high-frequency region, indicating that the charge-transfer resistance is negligible and that the electrode–electrolyte interface is highly conductive. The nearly unchanged intercept on the real axis before and after cycling confirms that the solution/internal resistance (R_s) remains stable, reflecting the structural integrity of the electrode and the robustness of the current collector–electrode contact. Importantly, the low-frequency region evolves toward a more vertical line after cycling, suggesting a transition toward more ideal capacitive behavior with reduced ion diffusion resistance. This improvement implies electrolyte wetting and progressive activation of electrochemically accessible sites during cycling. Overall, the minimal change in R_s and the enhanced low-frequency capacitive response collectively demonstrate fast charge transport, suppressed interfacial degradation, and excellent electrochemical stability of the FZMn-15 electrode upon prolonged cycling. The FZMn-15||AC asymmetric device was subjected to prolonged charge–discharge testing up to 15 000 cycles, as shown in Fig. 8e. Remarkably, the device retained 92% of its initial capacitance along with a coulombic efficiency of 99%, underscoring its excellent electrochemical reversibility and long-term operational stability. Such outstanding cycling performance highlights the practical applicability of FZMn-15 as a superior electrode material for high-performance supercapacitor devices. The fabricated FZMn-15||AC asymmetric device delivers a power density of 750 W kg^{-1} along with an energy density of 29 Wh kg^{-1}. These values highlight the device's ability to maintain

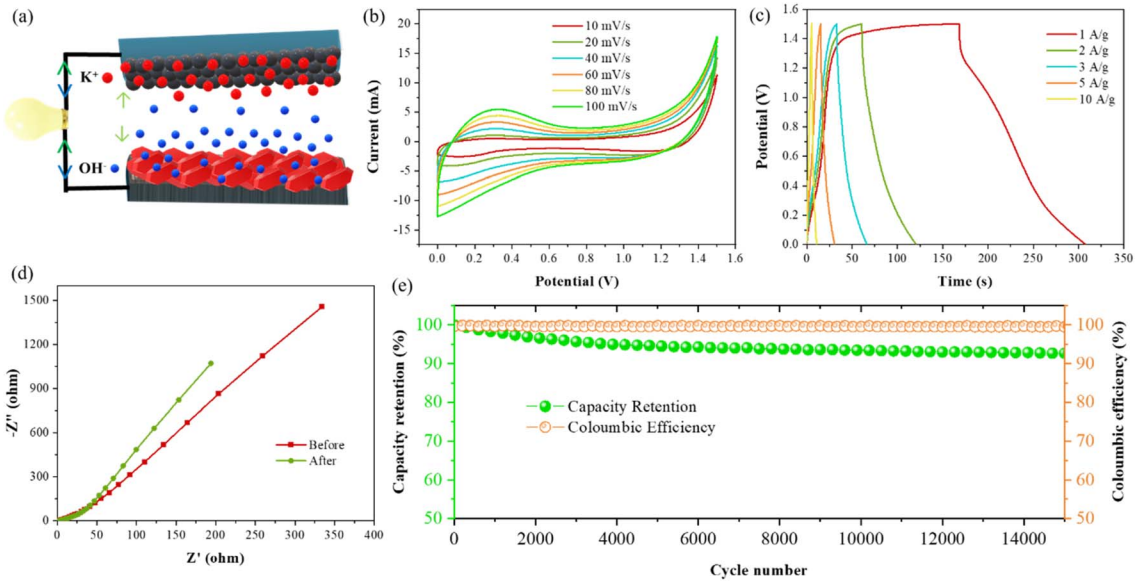

Fig. 8 (a) Schematic illustration of the FZMn-15||AC device; (b and c) CV and GCD curves, (d) before and after cycling EIS spectra and (e) long-term cycling stability of the FZMn-15||AC device.

a favorable balance between high energy storage capability and rapid power delivery, underscoring its potential for practical high-performance supercapacitor applications. The Ragone plot, comparing the energy and power densities of the fabricated electrodes with previously reported systems, is provided in the supplementary information (Fig. S5). Further, the stability of the material was confirmed by post-cycling XRD and SEM analyses (Fig. S5 and S6), consistent with previously reported studies.[40,41] The detailed discussion of the post-cycling XRD and SEM results is provided in the SI.

5 Conclusion

In this study, FZMn-15 emerged as the optimized electrode composition, demonstrating superior electrochemical characteristics compared to the other variants FZMn-0, FZMn-1, FZMn-5, FZMn-10 and FZMn-20. In the three-electrode configuration, FZMn-15 delivered a specific capacitance of 1531 F g^{-1} at 1 A g^{-1}, retaining 896 F g^{-1} even at 10 A g^{-1}, reflecting its outstanding rate capability. The asymmetric device FZMn-15||AC, delivered a specific capacitance of 92 F g^{-1}, with a discharge time of 308 s at 10 A g^{-1}, confirming its practical applicability. Furthermore, the device exhibited a power density of 750 W kg^{-1} and an energy density of 29 Wh kg^{-1}, striking a strong balance between energy storage capacity and rapid power delivery. Mechanistic studies revealed that the charge storage process in FZMn-15 is predominantly diffusion-controlled as confirmed by *b* value calculation. Along with the capacitive–diffusive contribution analysis, which revealed a gradual transition from surface-controlled to diffusion-dominated behavior with increasing scan rate. This distinctive hybrid charge storage mechanism, enabled by optimal Mn incorporation, ensures efficient ion transport, reduced resistance and robust structural integrity, thereby delivering outstanding capacitance retention and coulombic efficiency.

Author contributions

P. R.: writing – original draft, writing – review & editing, methodology, investigation, data curation, conceptualization. V. T., N. M. C. & M. S. I.: writing – review & editing, methodology, data curation, conceptualization. M. P. & I. P.: writing – review & editing, formal analysis. K. Y.: resources, formal analysis. S.-H. K.: project administration, funding acquisition, formal analysis. J. K.: validation, supervision, project administration, funding acquisition.

Conflicts of interest

The authors declare that they have no known competing financial interests or personal relationships that could have appeared to influence the work reported in this paper.

Data availability

Supplementary information (SI): equations for mass ratio calculations, capacitance and efficiency evaluations, power-law model analysis, X-ray photoelectron spectroscopy (XPS) plot, electrochemical impedance spectroscopy (EIS) results, stability studies of the FZMn-15 electrode, and the Ragone plot comparing the present work with reported literature. See DOI: https://doi.org/10.1039/d5ta08979d.

Acknowledgements

This work was supported by Nano Material Technology Development Program (grant no. RS-2024-00408180) through the

National Research Foundation (NRF) of Korea funded by the Ministry of Science, ICT, and Future Planning.

References

1 K. R. Ngoy, V. T. Lukong, K. O. Yoro, J. B. Makambo, N. C. Chukwuati, C. Ibegbulam, O. Eterigho-Ikelegbe, K. Ukoba and T. C. Jen, *Renew. Sustain. Energy Rev.*, 2025, **223**, 115971.
2 J. R. Miller and P. Simon, *Science*, 2008, **321**(5889), 651–652.
3 Y. Wang, Y. Song and Y. Xia, *Chem. Soc. Rev.*, 2016, **45**(21), 5925–5950.
4 S. Karthikeyan, B. Narenthiran, A. Sivanantham, L. D. Bhatlu and T. Maridurai, *Mater. Today: Proc.*, 2021, **46**, 3984–3988.
5 M. S. Iyer and R. Ilangovan, *ACS Appl. Energy Mater.*, 2023, **6**(7), 3682–3695.
6 P. Rajkumar, V. Thirumal, G. Radhika, K. Yoo and J. Kim, *Biomass Convers. Biorefinery*, 2024, **14**, 30707–30717.
7 M. S. Iyer and I. Rajangam, *Colloid Interface Sci. Commun.*, 2022, **46**, 100577.
8 P. Paunkumar, A. Sasmal, A. K. Nayak and S. G. Babu, *J. Solid State Electrochem.*, 2024, **28**(7), 2071–2079.
9 P. Rajkumar, V. Thirumal, M. S. Iyer, M. Abdollahifar, K. Aravinth, K. Yoo and J. Kim, *J. Ind. Eng. Chem.*, 2024, **134**, 102–111.
10 M. S. Iyer and I. Rajangam, *J. Energy Storage*, 2023, **67**, 107530.
11 R. Vinodh, R. S. Babu, S. Sambasivam, C. V. M. Gopi, S. Alzahmi, H. J. Kim, A. L. F. de Barros and I. M. Obaidat, *Nanomaterials*, 2022, **12**(9), 1511.
12 S. Asaithambi, P. Rajkumar, A. S. Rasappan, G. Ravi, D. Velauthapillai, K. Yoo and J. Kim, *J. Energy Storage*, 2023, **72**, 108532.
13 Y. Dai, H. Gul, C. Sun, L. Tan, Y. Guo, W. Raza, A. Hussain, J. Pan, M. Azam, W. Zhu and B. Chen, *Electrochim. Acta*, 2023, **438**, 141575.
14 P. Paunkumar, A. Sasmal, A. K. Nayak and S. G. Babu, *J. Solid State Electrochem.*, 2024, **28**(7), 2071–2079.
15 R. Barik, B. K. Jena and M. Mohapatra, *RSC Adv.*, 2017, **7**(77), 49083–49090.
16 Z. Luo, J. Quan, T. Ding, B. Xu, W. Li, Q. Mao, W. Ma, M. Li, H. Xiang and M. Zhu, *J. Alloys Compd.*, 2024, **980**, 173614.
17 B. Guo, H. Huo, Q. Zhuang, X. Ren, X. Wen, B. Yang, X. Huang, Q. Chang and S. Li, *Adv. Funct. Mater.*, 2023, **33**(25), 2300557.
18 S. Liu, Y. Zhang, L. Hao, A. Nsabimana and S. Shen, *Sep. Purif. Technol.*, 2025, **354**, 129501.
19 D. Acharya, T. H. Ko, R. M. Bhattarai, A. Muthurasu, T. Kim, S. Saidin, J. S. Choi, K. Chhetri and H. Y. Kim, *Adv. Compos. Hybrid Mater.*, 2023, **6**(5), 179.
20 M. Li, L. Zhu, J. Wang, L. Ma, Z. Pan, W. Ji, X. Sun, R. Li, X. Li, S. Duan and Y. Tao, *Water*, 2024, **16**(13), 1795.
21 C. Liu, X. Kan, F. Hu, X. Liu, S. Feng, J. Hu, W. Wang, K. M. U. Rehman, M. Shezad, C. Zhang and H. Li, *J. Alloys Compd.*, 2019, **785**, 452–459.
22 A. Gupta and P. K. Roy, *Inorg. Chem. Commun.*, 2023, **155**, 111114.
23 Z. Guo, Y. Ma, X. Dong, J. Huang, Y. Wang and Y. Xia, *Angew. Chem.*, 2018, **130**(36), 11911–11915.
24 A. T. Sami, S. M. AL-Jawad, N. J. Imran and K. Alghazali, *J. Sol-Gel Sci. Technol.*, 2025, **113**(3), 762–777.
25 V. Soundharrajan, J. Lee, S. Kim, D. Y. Putro, S. Lee, B. Sambandam, V. Mathew, K. Sakthiabirami, J. Y. Hwang and J. Kim, *Molecules*, 2022, **27**(24), 8664.
26 J. Zhang, H. Yuan, Z. Qin, P. Ding, D. Yu, H. Wu, J. Wang, Y. Shao, W. Zhou, C. W. Nan and Y. Ren, *Adv. Funct. Mater.*, 2025, **35**(3), 2413684.
27 J. Lee, D. A. Kitchaev, D. H. Kwon, C. W. Lee, J. K. Papp, Y. S. Liu, Z. Lun, R. J. Clément, T. Shi, B. D. McCloskey and J. Guo, *Nature*, 2018, **556**(7700), 185–190.
28 D. Han, Z. Song, B. Liu, X. Zhang, J. Liu, Y. Huang, C. Xing and J. Zhang, *J. Mol. Struct.*, 2025, **1349**(3), 143895.
29 K. Yang, C. Li, Q. Zhu, H. Wang and J. Qi, *Nanomaterials*, 2025, **15**(7), 524.
30 H. J. Ahn, M. J. Kwak, J. S. Lee, K. Y. Yoon and J. H. Jang, *J. Mater. Chem. A*, 2014, **2**(47), 19999–20003.
31 S. Ilican, *J. Alloys Compd.*, 2013, **553**, 225–232.
32 M. C. Biesinger, *Appl. Surf. Sci.*, 2022, **597**, 153681.
33 M. M. Vadiyar, S. S. Kolekar, N. G. Deshpande, J. Y. Chang, A. A. Kashale and A. V. Ghule, *Ionics*, 2017, **23**(3), 741–749.
34 M. Wang, K. Chen, J. Liu, Q. He, G. Li and F. Li, *Catalysts*, 2018, **8**(4), 138.
35 Z. Hou, P. Yan, B. Sun, H. Elshekh and B. Yan, *Results Phys.*, 2019, **14**, 102498.
36 H. Wang, M. Yuan, J. Zhang, Y. Bai, K. Zhang, B. Li and G. Zhang, *EES Catal.*, 2024, **2**(1), 324–334.
37 Z. Wang, R. Lin, Y. Huo, H. Li and L. Wang, *Adv. Funct. Mater.*, 2022, **32**(7), 2109503.
38 C. N. Mohan, S. Asaithambi, P. Vijayakumar, P. Rajkumar and J. Kim, *Ceram. Int.*, 2025, **51**, 35385–35394.
39 S. Asaithambi, P. Sakthivel, M. Karuppaiah, K. Balamurugan, R. Yuvakkumar, M. Thambidurai and G. Ravi, *J. Alloys Compd.*, 2021, **853**, 157060.
40 J. Chen, W. Li, R. Sun, L. Yan, S. Li, Z. Xu, X. Zeng and Y. Hu, *Adv. Energy Mater.*, 2025, **15**(41), e03298.
41 Y. Shao, J. Chen, T. Zhang, Y. Tao, J. Ning, W. Lu and Y. Hu, *Chem. Eng. J.*, 2025, **524**, 169181.